

In Search of a Data Driven Symbolic Multi-Fluid 10-Moment Model Closure

John Donaghy¹†, Kai Germaschewski¹

¹Space Science Center, University of New Hampshire, Durham, NH 03824, US

The inclusion of kinetic effects into fluid models has been a long standing problem in magnetic reconnection and plasma physics. Generally the pressure tensor is reduced to a scalar which is an approximation used to aid in the modeling of large scale global systems such as the Earth’s magnetosphere. This unfortunately omits important kinetic physics which have been shown to play a crucial role in collisionless regimes. The multi-fluid 10-moment model on the other-hand retains the full symmetric pressure tensor. The 10-moment model is constructed by taking moments of the Vlasov equation up to second order, and includes the scalar density, the vector bulk-flow, and the symmetric pressure tensor for a total of 10 separate components. Use of the multi-fluid 10-moment model requires a closure which truncates the cascading system of equations. Here we look to leverage data-driven methodologies to seek a closure which may improve physical fidelity of the 10-moment multi-fluid model in collisionless regimes. Specifically we use the Sparse Identification of Nonlinear Dynamics (SINDy) method for symbolic equation discovery to seek the truncating closure from fully kinetic particle-in-cell simulation data, which inherently retains the relevant kinetic physics. We verify our method by reproducing the 10-moment model from the PIC particle data and use the method to generate a closure truncating the 10-moment model which is analyzed through the nonlinear phase of reconnection.

1. Introduction

Magnetic reconnection is the process in which a magnetic field embedded in plasma undergoes a topological restructuring. This process, which converts the energy stored in magnetic fields into particle kinetic and thermal energy is ubiquitous throughout the universe and plays an important role in such diverse events as sawtooth crashes in fusion plasmas (Yamada 2010; Zweibel 2009), magnetic substorms in the earth’s magnetosphere (Hastie 1997), and solar coronal mass ejections (Masuda *et al.* 1994).

Magnetic reconnection was first studied using magnetohydrodynamics (MHD). In ideal MHD, which describes a plasma as a single fluid of infinite conductivity, Ohm’s Law in the lab frame is given by $\mathbf{E} + \mathbf{u} \times \mathbf{B} = \eta \mathbf{J} = 0$ and implies that magnetic flux is frozen into the plasma flows. Hence magnetic reconnection is topologically prohibited.

In real plasmas, however, the right-hand-side (r.h.s) of the Ohm’s Law is not zero. In resistive MHD, finite conductivity is introduced as the resistive term $\eta \mathbf{J}$. Sweet and Parker (Parker 1957) used this model to develop the first self-consistent description of magnetic reconnection. However, many plasmas of interest are nearly collisionless and the reconnection rates predicted by Sweet-Parker do not match observations. Petschek’s model (Petschek 1964) addressed the shortcomings of the Sweet-Parker model by realizing that the geometry of the reconnection region is crucial and that reducing the aspect ratio of that region can explain the observed faster reconnection rates. This means that the

† Email address for correspondence: john.donaghy@unh.edu

reconnection region does span the global length scale but is much shorter and connected to the global geometry by slow shocks. Petschek's model, however is not realized in numerical simulations unless one triggers a shorter reconnection region by anomalous resistivity or other modifications of the physics.

It was later realized that the one-fluid MHD description of plasmas is too limited to incorporate all the essential reconnection physics. The next steps were Hall-MHD and extended MHD models that take into account that electrons and ions do not move together at the small scales of a reconnection region. From the electron momentum equation, one can derive a generalized Ohm's Law (Vasyliunas 1975; Birn *et al.* 2001):

$$\mathbf{E} + \mathbf{u} \times \mathbf{B} = \eta \mathbf{J} + \frac{\mathbf{J} \times \mathbf{B}}{n|e|} - \frac{\nabla \cdot \mathbf{P}_e}{n|e|} + \frac{m_e}{n|e|^2} \times \left[\partial_t \mathbf{J} + \nabla \cdot \left(\mathbf{u} \mathbf{J} + \mathbf{J} \mathbf{u} - \frac{\mathbf{J} \mathbf{J}}{n|e|} \right) \right] \quad (1.1)$$

The generalized Ohm's law (1.1) describes the various non-ideal contributions to the electric field in a plasma. The resistive dissipation term, sometimes denoted as the collisional term, is given by $\eta \mathbf{J}$. The second term on the right hand side is called the Hall term which in and of itself cannot support magnetic reconnection. It is however known to change the geometry of the reconnection process to enable "fast" reconnection, where the time scales of the process are on the order of the Alfvénic transit times. The third term is the divergence of the electron pressure tensor, and the last term is the electron inertial term.

In fluid simulations, the electron pressure tensor is usually approximated by a scalar pressure, however it is known from fully kinetic simulations that off-diagonal terms can support reconnection electric fields. It has generally become clear that kinetic physics, being the first-principles description of a plasma, are important for a complete description of magnetic reconnection, in particular in the collisionless regime. Advances in computing power have enabled comparatively large fully kinetic simulations using the particle-in-cell (PIC) method, even in 3-d, that can achieve a good separation between the global size of the simulation and ion and electron scales, even though they usually require a reduced ion/electron mass ratio to keep the computational cost manageable. These kinds of simulations are limited to local simulations of reconnection, although their extent may be 10s or 100s of ion inertial scales (d_i). In contrast, many physical systems of interest, e.g., Earth's magnetosphere or the Sun's corona are many orders of magnitude larger and will remain inaccessible to fully kinetic simulations for the foreseeable future.

Fluid simulations are computationally cheaper than kinetic simulations and continuum codes, making them computationally more attractive but at the cost of a loss of kinetic information in the closure formulation.

An alternative fluid formulation employed in this context is the multi-fluid moment model. This model is derived without any approximations by taking moments of the Vlasov equation and keeps the full set of Maxwell's Equations.

1.1. Multi-Fluid and Ten Moment Model

$$d_t f_s = \partial_t f_s + \mathbf{v} \cdot \nabla_r f_s + \frac{q}{m} (\mathbf{E} + \mathbf{v} \times \mathbf{B}) \cdot \nabla_v f_s = 0 \quad (1.2)$$

The multi-fluid model is constructed by taking sequentially increasing velocity space moments of the Vlasov equation (1.2) for each species s . Following (Wang *et al.* 2015),

the following moments are defined:

$$n \equiv \int f d\mathbf{v} \quad (1.3a)$$

$$u_j \equiv \frac{1}{n} \int v_j f d\mathbf{v} \quad (1.3b)$$

$$\mathcal{P}_{ij} \equiv m \int v_i v_j f d\mathbf{v} \quad (1.3c)$$

$$\mathcal{Q}_{ijk} \equiv m \int v_i v_j v_k f d\mathbf{v} \quad (1.3d)$$

The evolution equations for these moments are derived by multiplying the Vlasov equation by consecutive powers of v and integrating out velocity space. Truncating the system of equations after the 2nd order gives the so-called 10-moment equations (1.4), which describe the evolution of density, the three components of momentum, and each of the 6 unique components of the symmetric pressure tensor. Each species is maintained as a separate set of fluid moments, but a species index has been left out above for brevity.

$$\partial_t n + \partial_j (n u_j) = 0 \quad (1.4a)$$

$$m \partial_t (n u_i) + \partial_j \mathcal{P}_{ij} = n q (E_i + \epsilon_{ijk} u_j B_k) \quad (1.4b)$$

$$\partial_t \mathcal{P}_{ij} + \partial_k \mathcal{Q}_{ijk} = n q u_{[i} E_{j]} + \frac{q}{m} \epsilon_{[ikl} \mathcal{P}_{kj]} B_l \quad (1.4c)$$

The square bracket notation above indicates the minimal sum over free indices that yields a completely symmetric tensor. The electromagnetic fields evolve according to the Maxwell equations

$$\nabla \times \mathbf{E} = -\frac{\partial \mathbf{B}}{\partial t} \quad (1.5a)$$

$$\nabla \times \mathbf{B} = \mu_0 \mathbf{J} + \frac{1}{c^2} \frac{\partial \mathbf{E}}{\partial t} \quad (1.5b)$$

Noticeably, each moment equation contains the next higher order moment. This trend continues ad-infinitum resulting in an open system of equations. While this system of equations is exact, it needs to be truncated, which in the ten-moment model is achieved by seeking a closure that removes the unknown \mathcal{Q} from the second order equation. This closure may be a function of the known ten moments or may be zeroed out completely for the adiabatic case, resulting in the 5-moment model. In this work, we are specifically interested in the pressure tensor term's impact on reconnection and hence choose to keep it.

The above moments (1.3) are generally used for the derivation of the ten moment model, however the centered moments (1.6) are frequently used for the closure because of their convenient physical interpretation as the pressure stress tensor and heat flux tensor.

$$P_{ij} \equiv m \int (v_i - u_i)(v_j - u_j) f d\mathbf{v} \quad (1.6a)$$

$$Q_{ijk} \equiv m \int (v_i - u_i)(v_j - u_j)(v_k - u_k) f d\mathbf{v} \quad (1.6b)$$

The centered and uncentered moments are related according to

$$\mathcal{P}_{ij} = P_{ij} + 2nm u_i u_j \quad (1.7a)$$

$$\mathcal{Q}_{ijk} = Q_{ijk} + u_i \mathcal{P}_{jk} - 2nm u_i u_j u_k \quad (1.7b)$$

Previous closures have been proposed such as the CGL family of closures (Chust & Belmont 2006) and the Hammett-Perkins closure (Hammett & Perkins 1990).

In this work we aim to use data-driven methodologies to derive a symbolic closure relation truncating the cascading system of equations at the 10-moment model.

We build off the work of (Wang *et al.* 2015), investigating the collisionless regime using data from a fully kinetic Harris Sheet PIC simulation. We then apply the data-driven technique, Sparse Identification of Nonlinear Dynamics (SINDy) (Brunton *et al.* 2016), to distill the raw particle output into a symbolic closure which is compared to the approximate local closure (1.8)

$$\partial_m Q_{ijm} \approx v_t |k_0| (P_{ij} - p \delta_{ij}) \quad (1.8)$$

In the above, v_t is the thermal velocity, k_0 is a typical scale defining wave number, p is the scalar pressure attained by averaging the diagonal of the pressure stress tensor, and the moments are centered. Originally defined in (Wang *et al.* 2015), (1.8) is referred to as the local approximate Hammett-Perkins closure because it is local in fourier space, using a single k value and is derived from the more general Hammett-Perkins closure.

In the literature various options for closures to the 10-moment model have been investigated (Ng *et al.* 2017, 2020) by implementing a given proposed closure into the multi-fluid moment model, choosing parameters like a typical wavelength of kinetic instability k_0 and running prototypical reconnection problems like the Harris sheet or island coalescence. The time evolution and snapshots of the fields are then compared to results of a particle-in-cell simulation.

In this work on the other hand, we exploit the additional information available from PIC simulations to test and derive closures. Since we do have the fully kinetic particle information available, we can for example calculate the third order heat flux moment and compare the actual heat flux observed in the simulation to the assumptions of a given closure. This process has the advantage that we can directly compare terms at any given time, whereas when comparing multi-fluid and PIC simulations, the state at any given time is an accumulation of all differences that have occurred up to this time.

2. Background

2.1. Particle-In-Cell Method

The Particle Simulation Code (PSC) (Germaschewski *et al.* 2016) is a modern, load-balanced, GPU accelerated, fully-kinetic particle-in-cell code. The PIC method is a numerical method which discretizes the electromagnetic fields on a 3D grid and advances them using Maxwell's equations while approximating the particle distribution function through macroparticles which are advanced in continuous phase space.

As a fully kinetic algorithm, the PIC method retains the full structure of the electron pressure tensor. Thus the PIC method exactly satisfies the 10-moment model up to noise. Systemic noise inherent to the PIC method is introduced primarily through the sampling of macroparticles to construct distribution functions.

This systemic noise was demonstrated to be a significant problem when applying the SINDy method to PIC data by (Alves & Fiuza 2020). By spatially integrating the PIC

data, they were able to reduce noise and apply SINDy to effectively recover the Vlasov equation. In §3 we borrow this technique and apply it to each of the moments and fields output by PSC before any further operation is performed.

2.2. Sparse Identification of Non-Linear Dynamics

The Sparse Identification of Non-Linear Dynamics is a framework for the discovery of symbolic equations. Developed by (Brunton *et al.* 2016), it looks to construct parsimonious solutions from a library containing candidate terms which are calculated from raw data. It may be used to take data from either experiment or simulation and generate symbolic governing equations which describe a dynamical system.

This is accomplished by solving the sparsity-promoting regression problem

$$\mathcal{L} = \min_{\mathbf{w}} \|\Theta\mathbf{w} - \mathbf{y}\|_2 + \lambda R(\mathbf{w}) \quad (2.1)$$

Where Θ is the library containing candidate terms, \mathbf{w} is the vector of coefficients associated with each term in the library, \mathbf{y} is the regression target, and $R(\mathbf{w})$ is some regularization function on \mathbf{w} scaled by constant λ . Commonly R is the L_1 -norm in which case the above becomes Lasso regression. For a detailed description of the framework, see (Zheng *et al.* 2019; Champion *et al.* 2020).

Our experiments approximate (2.1) by solving the least squares problem with thresholding. This involves iteratively solving the least squares problem $y = \Theta\mathbf{w}$ and applying an upper and lower bounded threshold to the discovered \mathbf{w} , thus restricting the coefficients to a pre-specified range.

The success of SINDy discovering a parsimonious equation is dependent on selecting an upper and lower bounds which maximally encourages sparse solutions while minimally allowing error. Solutions to problems of this sort are known as pareto-optimal if the family of solutions can not improve on one measure without hindering the other. In other-words, the optimal bounds for the thresholded least squares problem are associated with the solution that lives on the pareto-front where the number of included terms may not be further minimized without increasing the solution error.

Thus, for each instance in which we apply SINDy, we first solve the thresholded least squares problem with various bounds to construct the pareto curve. The optimal bounds are then selected from the pareto-front and the problem is re-solved with those bounds.

This method was selected to symbolically model our closure because it is fully interpretable, emulates nature by leveraging parsimony, and has previously been used successfully to model MHD systems (Alves & Fiuza 2020; Kaptanoglu *et al.* 2021).

3. Experiments

3.1. Harris Sheet Simulation

This study uses the PSC to simulate a collisionless Harris sheet reconnection problem. Initially in kinetic equilibrium, the magnetic field is initialized as $\mathbf{B} = B_0 \tanh(y/\lambda_B)\hat{\mathbf{x}}$ and the densities as $n_e = n_i = n_0 \operatorname{sech}^2(y/\lambda_B) + n_b$. The magnetic field is then given a small sinusoidal perturbation which initiates the reconnection process.

The run uses a 1280×640 grid with a mass ratio of 25 and 16×10^9 particles which resolves to $0.676 \Delta x/\text{Debye}$ length.

This simulation uses an abnormally high number of particles per cell for each species, approximately 10,000. This was done to lower the level of noise inherent to PIC methods.

L_x/d_{i0}	L_y/d_{i0}	L_z/d_{i0}	n_b/n_0	T_{i0}/T_{e0}	λ_B/d_{i0}
25	1	12.5	0.3	5	0.5

TABLE 1. Harris Sheet Simulation Numerical Parameters

3.2. Method

Our method, which relies on SINDy at its core, was used for verifying the ten moment model, analysing the existing local approximate Hammett-Perkins closure, and searching for an improved closure.

We begin by loading the moment and field data generated by PSC, which we spatially integrate with a 3x3 kernel. We then calculate relevant spatial and temporal derivatives on the data and construct a library of terms consisting of every r.h.s term from the 10-moment model. For each order we select out only terms with consistent units, for example the 2nd order equation’s library will contain all r.h.s terms from each of the six 2nd order equations. This acts as an a-priori constraint on which terms may be accepted into the library.

With the constructed library we then calculate the l.h.s of each equation in the 10-moment model. For consistency, we consider the l.h.s to be the derivative containing terms of the equation, with the exception of the 0th order where the partial time derivative is the l.h.s and the particle divergence is the r.h.s

The l.h.s is then used as a regression target wherein we apply the SINDy framework on the associated term library to discover the associated symbolic equations constituting the r.h.s. This method is summarized in algorithm 1.

Algorithm 1 Equation Synthesis

- 1: $E, B, f^i \leftarrow$ Load field and moment data, integrate
 - 2: Calculate $\partial_t f^i, \partial_x f^i, \partial_y f^i, \partial_z f^i$ for relevant moments
 - 3: Construct term library Θ
 - 4: define l.h.s as regression target
 - 5: Apply SINDy with pareto-optimal bounds
 - 6: **return** symbolic equation
-

3.3. Ten Moment Model and Method Verification

As the multi-fluid moment equations (1.4) are exact, we can verify them directly from the Harris sheet PIC data. To show this we individually calculate the left hand side (l.h.s) and right hand side (r.h.s) of each equation and demonstrate their equivalence.

In the following analysis we use the antisymmetric normalized L_2 error (3.1) as a method for four separate comparisons. The first is the numerical error between the l.h.s and r.h.s calculated directly from the PIC simulation data. This metric is used to verify that the kinetic data satisfies the 10-moment model and gives an indicator of the residual noise in the data after integration. The second comparison is the numerical error between the r.h.s calculated directly from the data and the discovered r.h.s equation applied to the data. This is an indicator for how well our method is able to reproduce theory. The third comparison is the numerical error between the l.h.s calculated from the data and the discovered r.h.s equation applied to the data, which gives an indicator for how well our discovered equation can explain the l.h.s of each moment relation.

r.h.s	discovered	$ L_2(\text{l.h.s, r.h.s}) $	$ L_2(\text{r.h.s, discovered}) $	$ L_2(\text{l.h.s, discovered}) $	coefficient error
$ \nabla \cdot (n\bar{u}) $	$ -1.06\partial_x nu_x - 1.07\partial_z nu_z $	0.234	0.071	0.225	0.065

TABLE 2. The true r.h.s, discovered r.h.s, and systematic errors of the 0th order moment equation.

The final comparison we make is the normalized L_2 metric between the coefficients given by the known multi-fluid equations (1.4) and those discovered using the regression method. This is referred to as the coefficient error.

$$L_2(\mathbf{x}_1, \mathbf{x}_2) = \frac{\|\mathbf{x}_1 - \mathbf{x}_2\|_2}{\|\mathbf{x}_1\|_2} \quad (3.1)$$

Using this analysis we find that the regression method is able to reproduce the multi-fluid equations if the $L_2(\text{l.h.s, discovered})$ error is equal to or approximately equal to the $L_2(\text{l.h.s, r.h.s})$ error. Ultimately we are looking for symbolic, not numeric closure approximations. With this in mind the coefficient error is the truest indicator for the success of the method in reproducing (1.4).

Systematic error is introduced into the analysis when approximating the time and space derivatives with the centered finite-difference method. This error appears in the $L_2(\text{l.h.s, r.h.s})$ and the $L_2(\text{l.h.s, discovered})$ errors presented in the analysis and does not indicate a violation of the conservation laws.

We present our findings in tables 2 to 4 and figs. 1 to 3, where the data presented is from a representative step T-1699, during the nonlinear phase of reconnection. Experiments were run at various timesteps throughout the nonlinear phase and the results were shown to not differ greatly.

We note that the method verification of §3.3 was repeated for each equation using only the partial time derivative term as the regression target. Noise induced by the spatial derivatives did not pose a problem in r.h.s discovery. The derivative terms were found with similarly low error, justifying our use of the derivative containing terms as the l.h.s for semantic consistency.

3.3.1. 0th Order Verification

The 0th order equation, calculated from kinetic data, is verified visually as seen by the close matching in fig. 1 and the low $L_2(\text{l.h.s, r.h.s})$ error. One might believe that the residual noise would distort the ability of SINDy to isolate the correct dynamics. This however is not the case as demonstrated by the low coefficient error, 0.065. This demonstrates the robustness of this method to residual noise and the derivative approximation systematic error. This is important for validating the approach for use in closure discovery where many library terms will contain derivatives.

3.3.2. 1st Order Verification

The inclusion of field terms in the 1st order equations stabilizes the numerics significantly. This is demonstrated by the superb l.h.s-r.h.s matching, the low $L_2(\text{l.h.s, r.h.s})$ error, and the low $L_2(\text{l.h.s, discovered})$ error for each of the three components. Similarly, from the coefficient error we see that the method was able to reproduce the 1st order equations with 0.01-0.03 normalized L_2 coefficient error. These are strong results which

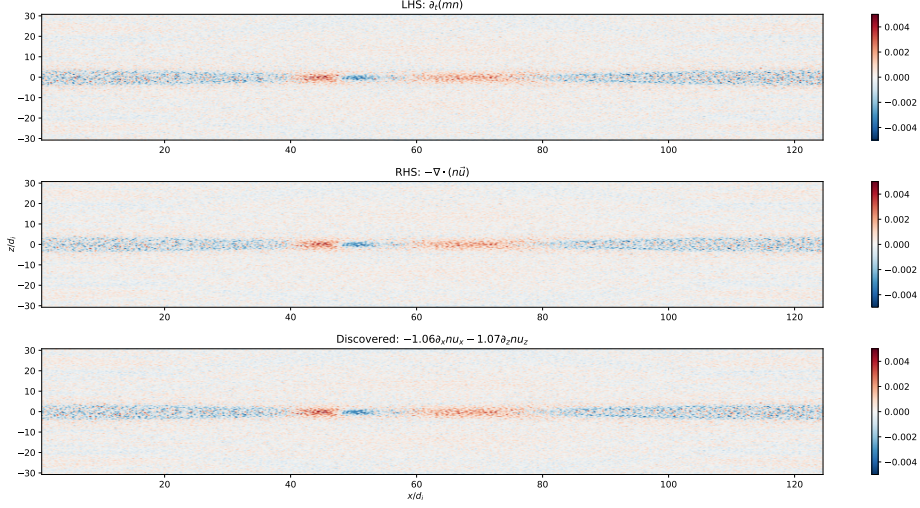


FIGURE 1. The 0th order moment equation or the continuity equation verified from the harris sheet PIC data. Here we contrast the l.h.s in the top pane with the true r.h.s in the center pane and the discovered r.h.s in the bottom pane

component	r.h.s	discovered	$ L_2(\text{l.h.s, r.h.s}) $	$ L_2(\text{r.h.s, discovered}) $	$ L_2(\text{l.h.s, discovered}) $	coefficient error
x	$ qnE_x + qn(\bar{u} \times \vec{B})_x $	$ 0.99qnE_x + 0.99qnu_yB_z - 1.05qnu_zB_y $	0.113	0.008	0.113	0.030
y	$ qnE_y + qn(\bar{u} \times \vec{B})_y $	$ 0.99qnE_y - 0.99qnu_xB_z + 0.99qnu_zB_x $	0.074	0.007	0.074	0.010
z	$ qnE_z + qn(\bar{u} \times \vec{B})_z $	$ 0.98nE_z + 0.97nu_xB_y - 0.98nu_zB_x $	0.044	0.014	0.041	0.023

TABLE 3. The true r.h.s, discovered r.h.s, and systematic errors for each component of the 1st order moment equations.

component	r.h.s	discovered	$ L_2(\text{l.h.s, r.h.s}) $	$ L_2(\text{r.h.s, discovered}) $	$ L_2(\text{l.h.s, discovered}) $	coefficient error
xx	$2j_xE_x + 2qP_{xy}B_z - 2qP_{xz}B_y$	$1.66j_xE_x + 1.80qP_{xy}B_z - 1.81qP_{xz}B_y$	0.215	0.084	0.195	0.126
yy	$2j_yE_y - 2qP_{yx}B_z + 2qP_{yz}B_x$	$2.05j_yE_y - 1.78qP_{yx}B_z + 1.93qP_{yz}B_x$	0.213	0.110	0.183	0.068
zz	$2j_zE_z + 2qP_{zx}B_y - 2qP_{zy}B_x$	$2.01j_zE_z + 2.07qP_{zx}B_y - 1.84qP_{zy}B_x$	0.288	0.093	0.272	0.050
xy	$ j_xE_y + j_yE_x + qP_{xy}B_z - qP_{yx}B_z - qP_{xz}B_y + qP_{zx}B_x $	$1.10j_xE_y + 0.87j_yE_x + 0.85qP_{xy}B_z - 0.86qP_{yx}B_z + 0.87qP_{xz}B_y - 0.87qP_{zx}B_x$	0.174	0.122	0.107	0.425
xz	$ j_xE_z + j_zE_x + qP_{xz}B_y + qP_{zx}B_y - qP_{yz}B_x - qP_{zy}B_x $	$0.86j_xE_z + 2.05j_zE_x + 3.06qP_{xz}B_y + 0.96qP_{zx}B_y - 0.97qP_{yz}B_x - 0.87qP_{zy}B_x$	0.128	0.106	0.053	0.947
yz	$ j_yE_z + j_zE_y + qP_{yz}B_x - qP_{zy}B_x + qP_{zx}B_z - qP_{xz}B_z $	$0.74j_yE_z - 1.48qP_{yz}B_x + 0.88qP_{zx}B_z - 0.87qP_{xz}B_z$	0.212	0.151	0.123	0.623

TABLE 4. The true r.h.s, discovered r.h.s, and systematic errors for each component of the 2nd order moment equations.

validate both the use of kinetic data for use in the 10-moment model and the use of SINDy to discover dynamics using the data.

3.3.3. 2nd Order Verification

The 2nd order equations demonstrate different behavior on-diagonal vs off-diagonal. The $L_2(\text{l.h.s, r.h.s})$ numerical errors are low in both the on-diagonal and off-diagonal terms, validating the 2nd order equations of the 10-moment model. Similarly the low

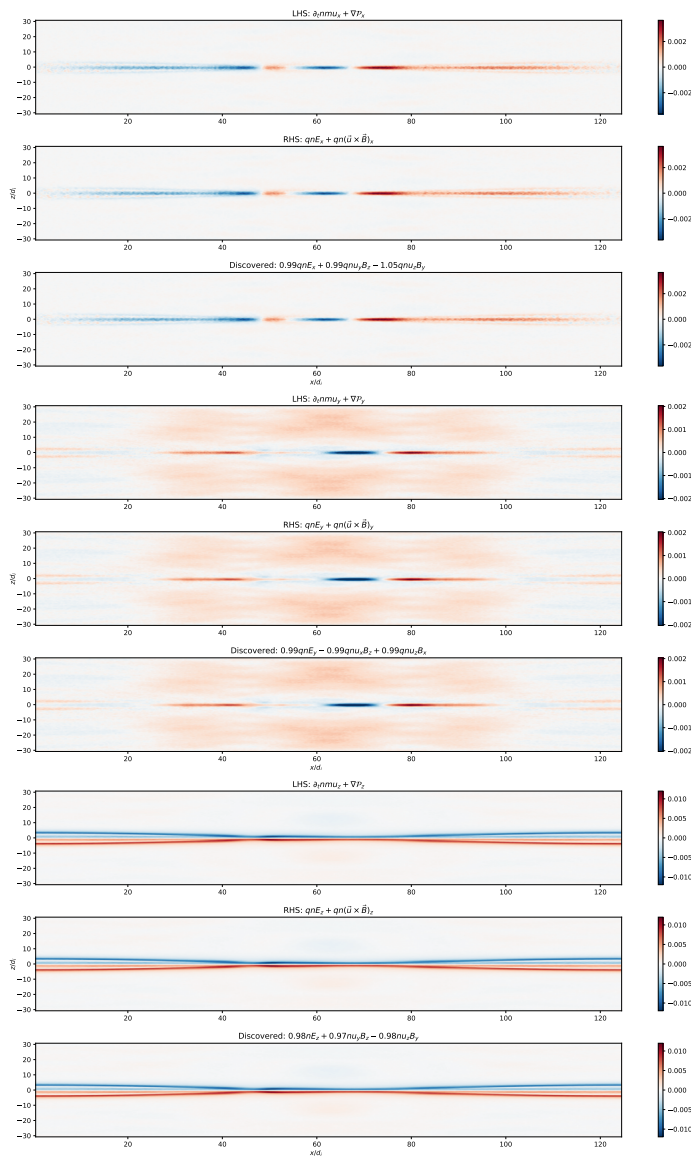


FIGURE 2. Top to bottom are the x-component, y-component, and z-component of the 1st order (momentum) equation with the l.h.s in the top pane, the true r.h.s in the middle pane, and the discovered r.h.s in the bottom pane

$L_2(\text{r.h.s, discovered})$ in conjunction with the low $L_2(\text{l.h.s, discovered})$ numerical error indicates that the terms included in the discovered solution account for the major contributions to the true r.h.s for each component. This similarly implies that the terms excluded from the discovered r.h.s must be of small magnitude. The small magnitude of these terms leads to discrepancies in the discovered r.h.s of the xy, xz, and yz directions, where the coefficient error is > 0.4 . This high coefficient error is due to the exclusion of terms from the discovered solutions. Any term with a small magnitude will be eliminated by SINDy and is a constraint of the method. Thus this inconsistency is explainable and expected in the case of minorly contributing terms.

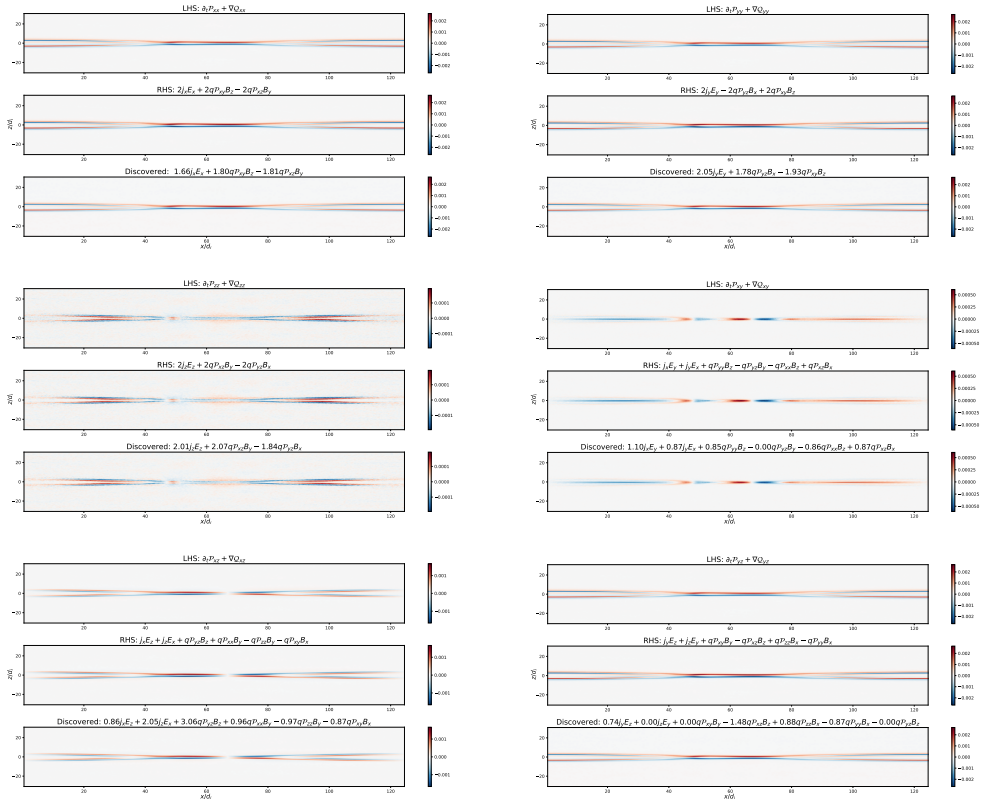


FIGURE 3. Top to bottom, left to right are the xx, yy, zz, xy, xz, yz components of the 2nd order moment equation. Each contains the regression target in the top pane, the true r.h.s in the center pane, and the discovered relation in the bottom. Visually, the l.h.s, r.h.s, and discovered source term of each component match well and are consistent with theory. This is true of both the on-diagonal and off-diagonal terms which demonstrates the reliability of our data. While some off-diagonal discovered terms may be missing, this is most likely due to their magnitude being small in this particular scenario.

3.4. Local approximate Hammett-Perkins Closure

The local closure (1.8) replaces the continuous wave-number k in the Fourier space response with just one typical wave-number k_0 . Thus, omitting k_0 when calculating the closure we would expect the l.h.s and r.h.s to differ by a constant factor. Further the closure is most important near the reconnection x-point where we expect important departures from ideal behavior. Generally, these trends seem to be verifiable in the kinetic data seen in fig. 4, there is however room for improvement in several areas. One obvious discrepancy is that each direction of the heat-flux divergence tensor scales by a different k_0 from the closure. Second is the clear disparity between the heat-flux divergence and the closure at regions of the domain distant from the x-point.

Each component presented in fig. 4 is represented with k_0 calculated by taking the average $\frac{\nabla Q_{ij}}{v_t(P_{ij} - p\delta_{ij})}$ across the entire domain. In all cases this results in the pressure terms being washed out with a lower magnitude than the heat flux divergence. The on-diagonal terms appear to match structurally while the off-diagonal terms differ. ∇Q_{xy} has some quadrupolar structure while the pressure terms appear to be bipolar. The large

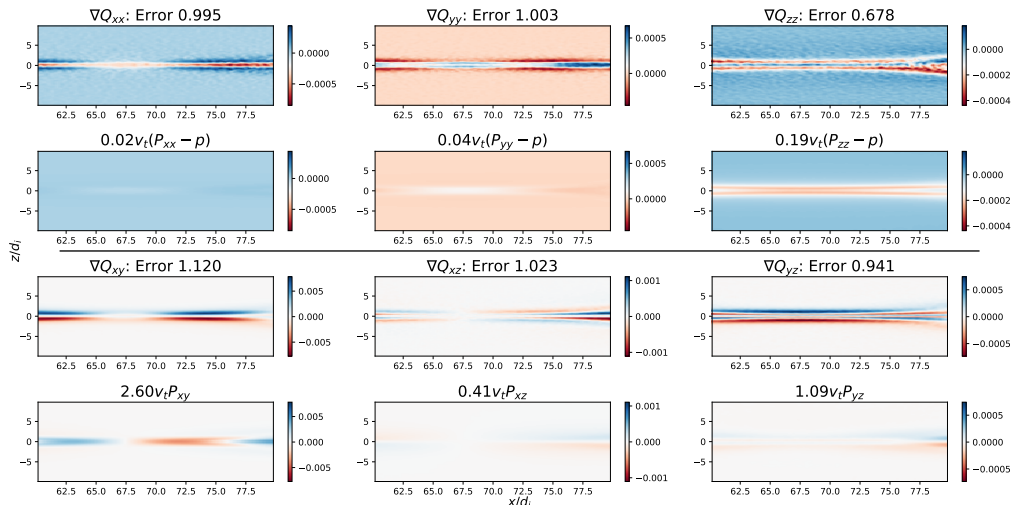


FIGURE 4. The local approximate Hammett-Perkins closure calculated during the nonlinear phase of reconnection. In each coordinate, the top row shows the divergence of the heat flux, while the bottom row represents the prediction of the approximate closure. The unknown factor k_0 for each component has been calculated by averaging $\frac{\nabla Q_{ij}}{v_t(P_{ij} - p\delta_{ij})}$ across the entire domain.

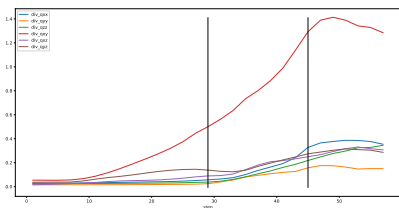


FIGURE 5. The L-2 Norm of each component of the heat flux divergence tensor, taken across the entire simulation domain. Vertical bars represent the nonlinear phase of reconnection.

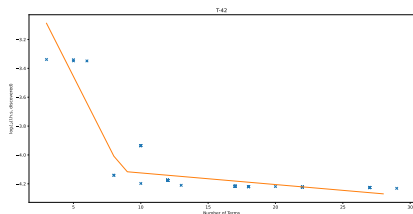


FIGURE 6. A representative Pareto curve constructed by solving SINDy with various upper and lower bounds for the yy -component of heat flux divergence. The bounds that yield the elbow are selected for model discovery.

scale structures of ∇Q_{xz} and ∇Q_{yz} are represented in the associated pressure terms, but the fine scale structures are omitted.

These discrepancies are significant and can lead to issues with physical fidelity when put into practical use as part of the 10-moment model.

3.5. Closure Discovery

Applying our methodology to the improvement or replacement of the above given closure, we decided to restrict ourselves to the nonlinear phase of the reconnection process. This range may be seen in fig. 5. Pareto-optimal bounds are required for SINDy to discover a parsimonious solution. Constructing a separate Pareto curve for each element of ∇Q_{ij} , we modified algorithm 1 to that shown in algorithm 2. A representative Pareto curve used in discovery of the yy -component closure is shown in fig. 6.

In Θ we include each component of the pressure tensor scaled by the thermal velocity,

Algorithm 2 Equation Synthesis

- 1: $E, B, f^i \leftarrow$ Load field and moment data, integrate
 - 2: Calculate $\partial_t f^i, \partial_x f^i, \partial_y f^i, \partial_z f^i$ for relevant moments
 - 3: Construct term library Θ
 - 4: **for** i, j **in** $\{x, y, z\} \times \{x, y, z\}$ **do**
 - 5: calculate pareto-optimal bounds
 - 6: define ∇Q_{ij} as regression target
 - 7: Apply SINDy
 - 8: **end for**
- return** symbolic equation

component	Hammett-Perkins	discovered	$L_2(\nabla Q_{ij}, \text{HP})$	$L_2(\nabla Q_{ij}, \text{discovered})$
xx	$ 0.02v_i(P_{xx} - p) $	$1.496k_0v_iP_{xx} + 3.067k_0v_iP_{yy} + 5.124k_0v_iP_{zz} - 2.499P_{xx}\partial_x u_x - 0.524j_x E_x - 1.372j_x E_y - 1.098j_x E_z + 1.174u_x\partial_x P_{xx} - 1.002u_x\partial_x P_{yy}$	0.995	0.604
yy	$ 0.04v_i(P_{yy} - p) $	$-1.393k_0v_iP_{xx} + 1.655k_0v_iP_{xx} + 0.854P_{xx}\partial_x u_x + 1.035P_{xx}\partial_x u_x + 0.621j_x E_x - 0.979u_x\partial_x P_{xx} - 2.999u_x\partial_x P_{xx} - 0.864u_x\partial_x P_{yy} + 4.233u_x\partial_x P_{zz}$	1.003	0.612
zz	$ 0.19v_i(P_{zz} - p) $	$0.619k_0v_iP_{xx} - 0.856k_0v_iP_{yy} - 0.476k_0v_iP_{zz} - 0.720P_{xx}\partial_x u_x + 0.442P_{xx}\partial_x u_x + 1.950P_{xx}\partial_x u_x - 1.437P_{xx}\partial_x u_x + 0.466j_x E_x + 0.415j_x E_y + 1.436j_x E_z + 1.147u_x\partial_x P_{xx} + 0.888u_x\partial_x P_{yy} - 0.833u_x\partial_x P_{zz}$	0.678	0.479
xy	$ 2.60v_iP_{xy} $	$-1.739k_0v_iP_{xx} - 0.524P_{xx}\partial_x u_x + 1.130P_{xx}\partial_x u_x - 0.702j_x E_x + 1.816u_x\partial_x P_{xx}$	1.120	1.000
xz	$ 0.41v_iP_{xz} $	$-2.135k_0v_iP_{xx} + 3.019P_{xx}\partial_x u_x - 5.953P_{xx}\partial_x u_x + 1.085u_x\partial_x P_{xx} - 1.962u_x\partial_x P_{xx}$	1.023	1.003
yz	$ 1.09v_iP_{yz} $	$-0.361k_0v_iP_{xx} + 2.420P_{xx}\partial_x u_x + 2.735P_{xx}\partial_x u_x + 0.208u_x\partial_x P_{xx} + 8.408u_x\partial_x P_{xx} - 3.029u_x\partial_x P_{xx} + 9.311u_x\partial_x P_{xx}$	0.941	0.999

TABLE 5. For each component of the heat flux divergence tensor we give the local approximate Hammett-Perkins closure, the discovered closure, and the relevant L_2 errors. The k_0 for each component of Hammett-Perkins is calculated by averaging $\frac{\nabla Q_{ij}}{v_t(P_{ij} - p\delta_{ij})}$ across the domain.

the energy transfer term $\mathbf{j} \cdot \mathbf{E}$, the Poynting flux terms $\nabla \cdot \mathbf{S}$, each component of the tensor $(\vec{u} \cdot \nabla)P$, and each term in the scalar product $(P\nabla) \cdot \vec{U}$. These terms were chosen for inclusion in Θ as each describes an energy flux and thus has the same physical units as heat flux divergence.

Table 5 summarizes our findings for a representative step (T-1699) during the nonlinear phase and fig. 7 demonstrates the temporal validity of the closure.

The analysis was repeated for various times through the nonlinear phase and the discovered solutions did not vary greatly. Errors for the discovered closure at evenly spaced times through the nonlinear phase are presented in the headers of fig. 7.

The on-diagonal closures were able to reduce the error significantly when compared to the given closure. The off-diagonal terms demonstrated no such improvement over the given Hammett-Perkins closure. However, our proposed closure comes with some caveats to be discussed further in §4.

4. Discussion and Conclusion

Fully kinetic data may be used to verify the 10-moment multi-fluid model as demonstrated up to and including 2nd order conservation laws. Specifically, 0th, 1st, and 2nd order equations were satisfied under visual inspection and with numerical error $L_2(\text{l.h.s}, \text{r.h.s}) \leq 0.28$ implying the multi-fluid 10-moment model may be validated with kinetic data. This is evidence that the SINDy methodology may be applied to kinetic data.

Applying the SINDy methodology, we were able to validate SINDy as a candidate data-driven approach up to and including the on-diagonal 2nd order terms as evidenced by the low L_2 coefficient error of the discovered solutions. Difficulties were encountered in the discovery of the off-diagonal 2nd order r.h.s terms (as demonstrated by high coefficient error), where the discovered solutions narrowly deviated from the conservation laws but found more parsimonious solutions with lower numerical error. This is due to the excluded

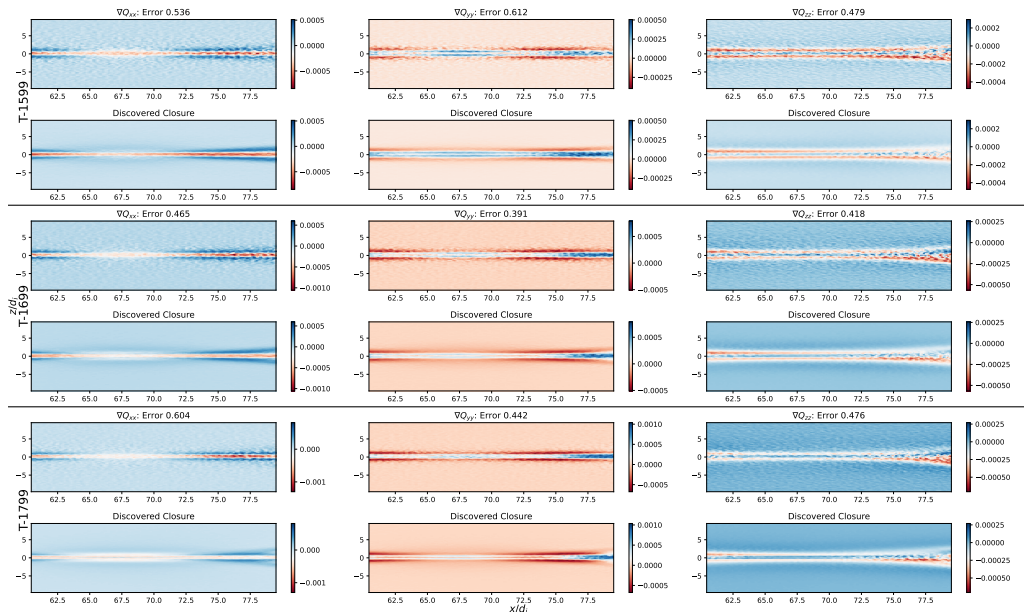


FIGURE 7. Snapshots of the discovered closure taken at intervals of 1000 w_{ce} throughout the nonlinear phase, represented row-wise. The diagonal components of ∇Q_{ii} are presented column-wise with the associated error in each of the headers. Of note is the consistent performance of the closure as the nonlinear phase progresses.

terms having a low order of magnitude leading to elimination by SINDy and not evidence of violation of the conservation laws.

Applied to heat flux divergence, this data-driven approach demonstrates strong results. The existing local approximate Hammett-Perkins closure gives us a baseline to measure improvement. The on-diagonal terms of the heat flux divergence were modeled with significantly reduced numerical L_2 error over the baseline. Furthermore the discovered closures appear to hold through a significant portion of the nonlinear phase as demonstrated in fig. 7. The off-diagonal terms were unsuccessfully modeled and further work is needed to understand this discrepancy.

Other shortcomings of this approach lie in perturbation phase restrictions. While the discovered closure holds well through the the nonlinear phase, there is no such guarantees during the linear phase. The local approximate Hammett-Perkins closure was derived using quasi-linear theory, as such we conjecture that the discovered closure will apply in the linear regime as well. Unfortunately we cannot demonstrate this at this time, due to the low signal-to-noise ratio in the linear phase.

As a data-driven method we make no attempt to explain the physics of the discovered closures here. Our sole claim is that the discovered closures will yield improved physical fidelity during the nonlinear phase when compared to eq. (1.8). Model validation is paramount when working with data driven methodologies, as such future directions in this research will involve applying the discovered closure to a multi-fluid simulation where we hope to see improvements over eq. (1.8). Further, we will be looking at expanding the methodology with the goal of pursuing a closure which accurately represents the off-diagonal terms.

REFERENCES

- ALVES, E. PAULO & FIUZA, FREDERICO 2020 Data-driven discovery of reduced plasma physics models from fully-kinetic simulations .
- BIRN, J., DRAKE, J. F., SHAY, M. A., ROGERS, B. N., DENTON, R. E., HESSE, M., KUZNETSOVA, M., MA, Z. W., BHATTACHARJEE, A., OTTO, A. & PRITCHETT, P. L. 2001 Geospace environmental modeling (gem) magnetic reconnection challenge. *Journal of Geophysical Research: Space Physics* **106** (A3), 3715–3719, arXiv: <https://agupubs.onlinelibrary.wiley.com/doi/pdf/10.1029/1999JA900449>.
- BRUNTON, STEVEN L., PROCTOR, JOSHUA L. & KUTZ, J. NATHAN 2016 Discovering governing equations from data by sparse identification of nonlinear dynamical systems. *Proceedings of the National Academy of Sciences* **113** (15), 3932–3937, arXiv: <https://www.pnas.org/content/113/15/3932.full.pdf>.
- CHAMPION, KATHLEEN, ZHENG, PENG, ARAVKIN, ALEKSANDR Y., BRUNTON, STEVEN L. & KUTZ, J. NATHAN 2020 A unified sparse optimization framework to learn parsimonious physics-informed models from data. *IEEE Access* **8**, 169259–169271.
- CHUST, T. & BELMONT, G. 2006 Closure of fluid equations in collisionless magnetoplasmas. *Physics of Plasmas* **13** (1), 012506.
- GERMASCHEWSKI, KAI, FOX, WILLIAM, ABBOTT, STEPHEN, AHMADI, NARGES, MAYNARD, KRISTOFOR, WANG, LIANG, RUHL, HARTMUT & BHATTACHARJEE, AMITAVA 2016 The plasma simulation code: A modern particle-in-cell code with patch-based load-balancing. *Journal of Computational Physics* **318**, 305–326.
- HAMMETT, GREGORY W. & PERKINS, FRANCIS W. 1990 Fluid moment models for landau damping with application to the ion-temperature-gradient instability. *Phys. Rev. Lett.* **64**, 3019–3022.
- HASTIE, R. J. 1997 Sawtooth Instability in Tokamak Plasmas. *Astrophysics and Space Science* **256** (1), 177–204.
- KAPTANOGLU, ALAN A., MORGAN, KYLE D., HANSEN, CHRIS J. & BRUNTON, STEVEN L. 2021 Physics-constrained, low-dimensional models for magnetohydrodynamics: First-principles and data-driven approaches. *Physical Review E* **104** (1).
- MASUDA, S., KOSUGI, T., HARA, H., TSUNETA, S. & OGAWARA, Y. 1994 A loop-top hard X-ray source in a compact solar flare as evidence for magnetic reconnection. *Nature* **371**, 495–497.
- NG, JONATHAN, HAKIM, AMMAR, BHATTACHARJEE, A., STANIER, ADAM & DAUGHTON, W. 2017 Simulations of anti-parallel reconnection using a nonlocal heat flux closure. *Physics of Plasmas* **24** (8), 082112, arXiv: <https://doi.org/10.1063/1.4993195>.
- NG, JONATHAN, HAKIM, A., WANG, L. & BHATTACHARJEE, A. 2020 An improved ten-moment closure for reconnection and instabilities. *Physics of Plasmas* **27** (8), 082106, arXiv: <https://doi.org/10.1063/5.0012067>.
- PARKER, E. N. 1957 Sweet’s mechanism for merging magnetic fields in conducting fluids. *Journal of Geophysical Research (1896-1977)* **62** (4), 509–520.
- PETSCHEK, HARRY E 1964 50 magnetic field annihilation. In *AAS-NASA Symposium on the Physics of Solar Flares: Proceedings of a Symposium Held at the Goddard Space Flight Center, Greenbelt, Maryland, October 28-30, 1963*, , vol. 50, p. 425. Scientific and Technical Information Division, National Aeronautics and . . .
- VASYLIUNAS, VYTENIS M. 1975 Theoretical models of magnetic field line merging. *Reviews of Geophysics* **13** (1), 303–336, arXiv: <https://agupubs.onlinelibrary.wiley.com/doi/pdf/10.1029/RG013i001p00303>.
- WANG, LIANG, HAKIM, AMMAR H., BHATTACHARJEE, A. & GERMASCHEWSKI, K. 2015 Comparison of multi-fluid moment models with particle-in-cell simulations of collisionless magnetic reconnection. *Physics of Plasmas* **22** (1), 012108.
- YAMADA, M. 2010 Magnetic reconnection. *Rev. Mod. Phys.* **82**, 603.
- ZHENG, PENG, ASKHAM, TRAVIS, BRUNTON, STEVEN L., KUTZ, J. NATHAN & ARAVKIN, ALEKSANDR Y. 2019 A unified framework for sparse relaxed regularized regression: Sr3. *IEEE Access* **7**, 1404–1423.
- ZWEIBEL, E. G. 2009 Magnetic reconnection in astrophysical and laboratory plasmas. *Annu. Rev. Astron. Astrophys.* **47**, 291.